Revealing out-of-equilibrium hidden phases in $Sr_3Ru_2O_7$ by applying stress

Pablo Rivero,[1,*] Vincent Meunier,[2] and William Shelton[1]

[1]*Center for Computation and Technology, Louisiana State University, Baton Rouge, Louisiana 70803, USA*

[2]*Department of Physics, Applied Physics, and Astronomy, Rensselaer Polytechnic Institute, Troy, New York 12180, USA*

We predict that the application of biaxial tensile strain will uncover an antiferromagnetic metallic *hidden phase* in $Sr_3Ru_2O_7$. By using hybrid density functional theory we applied uniaxial and biaxial strains and identified a variety of phases. We found that tensile strain can reduce by up to half the stress needed to expose hidden phases compared to the use of uniaxial compressive strain. In addition, our results demonstrate that while elongation and compression of the octahedra induce magnetic phase transitions, tilting of the octahedra leads to a metal-to-insulator transition, indicating that the different hidden phases can be accessed by applying strain.

I. INTRODUCTION

The search for hidden phases in complex materials is of significant importance to the materials community since it could lead to new structures that display fundamentally interesting and technologically desirable properties ranging from high-strength ductile alloys to colossal magnetoresistance and high-temperature superconductivity. In fact, hidden phases are a key ingredient for understanding materials under extreme environments (e.g., high pressure, temperature, strain, or high magnetic or electric fields) where controlling the behavior of materials driven far from their equilibrium is crucial for their performance under operating conditions. In addition, creating a surface can tip the delicate balance between the structural, charge, orbital, and spin degrees of freedom, thereby offering insights into uncovering possible hidden phases with sought-after properties in their corresponding bulk materials.

Creating a surface in $Sr_3Ru_2O_7$ breaks the inversion symmetry, which naturally occurs between the two double-octahedral layers. The most prominent effect at the surface is the octahedral tilt and increased rotation [1]. In our previous study we found that electronic and magnetic properties are not coupled with octahedra rotations, but tilting of the octahedra produces a less conducting state at the surface [2]. This result led us to apply uniaxial compressive strain along the [001] direction to force tilting of the octahedra throughout the structure, and we found two hidden phases. One transition is structural, where the *Bbcb* structure transforms into the *Bbmm* structure and leads to the emergence of octahedra tilts at 1.5 GPa, while the other involves a ferromagnetic (FM) metallic to antiferromagnetic (AFM) insulator phase transition at 21 GPa.

In this work we investigate the application of in-plane uniaxial and biaxial tensile strains on $Sr_3Ru_2O_7$. The study was motivated by our recent results on applying uniaxial compressive strain along the *c* axis where in-plane lattice parameters were progressively expanded, ultimately yielding to metal-to-insulator (MIT) and magnetic phase transitions [2].

This led us to the hypothesize that in-plane tensile strain could produce similar phase transitions but at a lower stress. Indeed, tensile strain not only reduces the stress needed to expose hidden phases compared to uniaxial compressive strain, but it also allowed us to uncover an AFM metallic hidden phase. Specifically, when tensile strain is applied along the [010] direction, the system undergoes the same structural phase transition but at a stress of only 0.6 GPa, while the FM metal to AFM insulator transition is predicted at $\simeq 17$ GPa and the AFM metallic phase is predicted at 10 GPa. The induced AFM phase is an AFM A-type state (AFM-A) that is characterized by Ru atoms that are coupled ferromagnetically in plane and antiferromagnetically out of plane in each bilayer of the system [Fig. 1(c)]. This AFM configuration is different from the ground-state AFM-I phase found in our previous investigation [3].

$Sr_3Ru_2O_7$ continues to attract much interest due to its wide range of interesting properties and intriguing phases, including metamagnetic transitions [4] and quantum critical phenomena [5]. Moreover, a certain number of parameters, including the amount and type of defects and alloying [6–11], pressure [12,13], temperature [14], and magnetic and electric fields [15], can give access to a wide range of electronic and magnetic properties. This is a consequence of the subtle interplay between charge, lattice, and spin degrees of freedom, which opens the possibility of controlling the properties of this compound. We will show here how applying strain on particular directions provides a way to control the structural properties of $Sr_3Ru_2O_7$ to induce a variety of phase transitions.

Neutron powder diffraction measurements and convergent-beam electron diffraction experiments on single crystals of $Sr_3Ru_2O_7$ found a *Bbcb* [16,17] (No. 68) orthorhombic space group structure with lattice parameters $a \simeq b$. In fact, there is another space group that describes this system as well, the *Pban* (No. 50) space group [18], which is a supergroup of the *Bbcb* space group. The advantage of using the *Pban* space group is that a larger number of AFM configurations can be generated for broader investigation of magnetic structures [3]. The bilayered perovskite is formed by two layers of RuO_6 octahedra connected by sharing one apical oxygen and separated by

---

*jprivero@lsu.edu
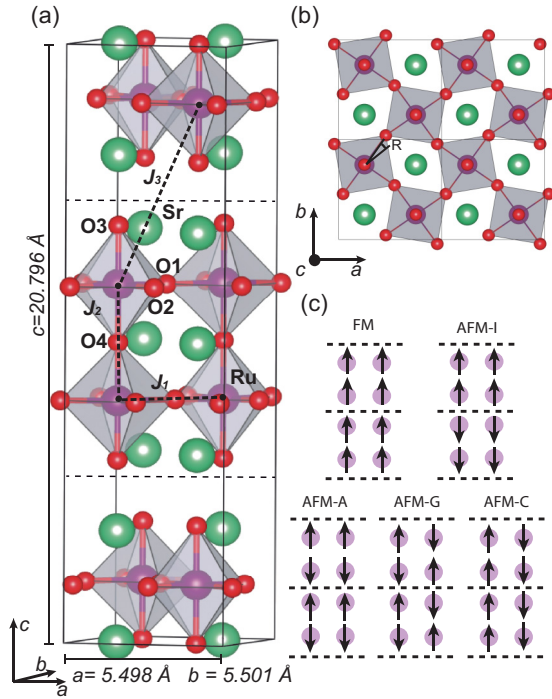
FIG. 1. Side and top views of the orthorhombic *Bbcb* structure of $Sr_3Ru_2O_7$. The RuO_6 octahedra are rotated alternately clockwise and counterclockwise about the c axis. Dashed lines delimit the $Sr_3Ru_2O_7$ bilayer. J_1, J_2, and J_3 are the magnetic couplings studied in this work. O1 and O2 refer to the in-plane oxygens, while O3 and O4 are the two different apical oxygens in the system. (b) Top view showing the octahedral rotations. R indicates the rotation angle. (c) Relevant magnetic phases studied in this work. The experimental cell parameters displayed were extracted from Ref. [16].

two SrO layers (Fig. 1). Each RuO_6 octahedral is rotated about the c axis by $7.855°$, while neighboring octahedra rotate by the same amount but in the counterclockwise direction [17]. It is important to recall here that in the bulk structure no octahedral tilts are observed.

Our study begins by presenting an extended and more detailed analysis of our previous investigation of uniaxial compressive strain. It allowed us to gain additional understanding of the coupling between degrees of freedom and contributed to the support of our hypothesis to apply in-plane tensile strain to expose hidden phases at a lower stress. We will show that the magnitude and direction of the strain applied to the system are key to inducing different hidden phases. Finally, a guide for experimentalists in search of hidden phases is provided.

II. COMPUTATIONAL DETAILS

We performed first-principles density functional theory calculations using the CRYSTAL14 computational package [19,20]. CRYSTAL14 employs atom-centered Gaussian-type orbital (GTO) basis sets to build Bloch functions, which are used to expand the one-electron crystalline orbitals. The GTO basis sets for each atom comprising the $Sr_3Ru_2O_7$ system were taken from Ref. [21]. For Ru and Sr, the small-core Hay-Wadt pseudopotentials [22] were adopted for the description of the inner-shell electrons ($1s^2 2s^2 2p^6 3s^2 3p^6 3d^{10}$).

The valence functions for Ru were based on the modified Los Alamos National Laboratory 2 double ζ (LANL2DZ) basis [23], $4s^2 4p^6 4d^7 5s^1$, while the $4s^2 4p^6 5s^2$ basis was used for Sr. Finally, for O atoms we used the 8-411d all-electron basis set constructed by Corà [24]. The effects of spin-orbit coupling and phonon properties have not been considered in this work. For all calculations we have used a hybrid functional based on a mixing of 10% Hartree Fock Exchange (HFX) with 90% revised Perdew-Burke-Ernzerhof GGA functional (PBESol) [25] exchange potential (PBES-10). This particular functional has been shown to accurately capture the electronic, magnetic, and structural properties of bulk [3] and surface $Sr_3Ru_2O_7$ [2].

For our calculations an $8 \times 8 \times 8$ Monkhorst-Pack mesh [26] was utilized to generate a 170-k-point sampling of the irreducible Brillouin zone. The thresholds controlling the accuracy in the evaluation of Coulomb and exchange integrals were set to 10^{-7} (ITOL1, ITOL2, ITOL3, and ITOL4, using notations from Ref. [20]) and 10^{-14} (ITOL5), while the self-consistent-field energy threshold was set to 10^{-6} a.u.

To study the electronic structure and magnetic properties of $Sr_3Ru_2O_7$ under uniaxial pressure, we performed a constrained geometry relaxation where we fixed the c lattice parameter and relaxed the a and b lattice parameters and all atomic coordinates. We manually changed the value of c to investigate the effect of different compressive strains applied parallel to the [001] direction on the electronic and magnetic properties. The study of the application of in-plane tensile strains was carried out for different values of the a and/or b lattice parameters, which we kept fixed while relaxing the c parameter and all atomic positions. The convergence criterion for gradient components and nuclear displacements in both studies was set to 0.0003 hartree/bohr and 0.0012 bohr, respectively. The total energy convergence threshold between geometry optimization steps was set to 10^{-6} hartrees. By using these parameters we obtain converged total energies within 1–2 meV per unit cell.

In this study, we consider only a homogeneous chemical and magnetic phase regardless of the amount of strain applied. Nevertheless, the real system may respond by decomposing the material into different polymorph phases or binary metal oxides ($Sr_{n+1}Ru_nO_{3n+1}$) [27,28].

The estimation of the uniaxial pressure applied to the system was obtained by analyzing the stress tensor as reported in the Supplemental Material of Ref. [2].

III. RESULTS AND DISCUSSION

Recent experimental measurements in $Sr_3Ru_2O_7$ indicate that the emergence of octahedral tilts at the surface drives the system towards a less conducting state than in the bulk [1]. The same study suggests that applying uniaxial compressive strain along the c axis in the bulk structure will stimulate the emergence of octahedral tilts in the entire structure, ultimately leading to a phase transition. Octahedra tilting starts to develop at $\simeq 1.5$ GPa of uniaxial pressure, while the MIT and magnetic phase transitions occur at a higher pressure of about 21 GPa.

To uncover hidden phases we first investigate the competition between different magnetic configurations as a function of compressive strain along the [001] direction by varying the c lattice parameter (Sec. III A). This allows us to determine the

TABLE I. Calculated a and b cell parameters (Å), volume V (Å^3), RuO$_6$ octahedra tilt and rotation (Rot) angles (degrees), and $\Delta EX = E_{\text{AFM}-X} - E_{\text{FM}}$ (meV) as a function of compressive strain along the c axis.

c	a	b	V	Rot	Tilt	ΔEA	ΔEG	ΔEC	ΔEI
20.796[a]	5.477	5.477	623.8	8.05	0.00				
20.73[b]	5.498	5.501	626.9	7.85	0.00				
20.6[c]	5.49	5.49	620.8	9.70	0.00	370	501	681	3.8
20.5	5.49	5.50	619.3	9.40	0.00	360			
20.4	5.51	5.51	619.7	8.97	0.00	354	527	608	
20.3	5.52	5.53	619.4	8.34	0.00	346			
20.2	5.51	5.61	624.2	2.1	8.56	338	264	735	
20.0	5.52	5.63	620.6	2.0	8.84	308	298	857	1.1
19.7	5.53	5.66	616.6	1.3	9.61	283	492	542	6.0
19.4	5.54	5.70	612.2	1.1	10.22	266			2.0
19.2	5.54	5.72	608.5	1.0	10.70	239	388	425	
18.9	5.55	5.77	604.8	1.0	11.66	151			
18.8	5.55	5.78	603.6	1.0	12.05	114	194	320	1.5
18.6	5.56	5.81	601.3	0.8	12.65	29	87	305	
18.5	5.64	5.85	610.4	0	12.55	−12	30	291	−6
18.4	5.65	5.87	610.1	0	12.45	−75	−43		
18.3	5.65	5.89	609.6	0	12.47	−125	−101		
18.2	5.66	5.91	608.5	0	12.65	−160	−151	258	−12
18.1	5.67	5.93	607.7	0	12.76	−230	−213		
18.0	5.68	5.94	607.4	0	12.80	−294	−270	155	−5

[a]Experimental results from Ref. [18].

[b]Experimental results from Ref. [16].

[c]Fully relaxed.

lowest energetic state as a function of strain. Then we study the structural (Sec. III B), magnetic, and electronic (Sec. III C) properties also as a function of uniaxial compressive strain to understand the physical mechanisms that trigger these phase transitions. The results obtained lead us to study an alternative procedure to drive the MIT and magnetic phase transitions in Sr$_3$Ru$_2$O$_7$ which consists of the application of in-plane tensile strains (Sec. III D).

A. Competition between different magnetic phases under uniaxial compressive strain

In this section we study the evolution of magnetism in the system as a function of uniaxial compressive strain along the c axis. The results obtained can provide hints about how to reproduce the reported hidden phases at a lower stress. We considered the FM phase and four different AFM spin orderings, which include the A, G, C, and I types of arrangements [see Fig. 1(c)]. The total energy difference between FM and AFM-X (where X is A, G, C, or I) displayed in Table I is defined as $\Delta EX = E_{\text{AFM}-X} - E_{\text{FM}}$.

Figure 2 displays the energy of the AFM-A, AFM-C, and AFM-G configurations as well as the FM state relative to the FM ground state as a function of decreasing c. On the one hand, we notice that total energies involving AFM-C are higher than other AFM phases when decreasing the c lattice parameter, and thus, it does not compete as a potential new state in the parameter range considered. On the other hand, the total energy of the AFM-I phase, which is characterized by FM bilayers coupled antiferromagnetically, is higher in energy than the FM
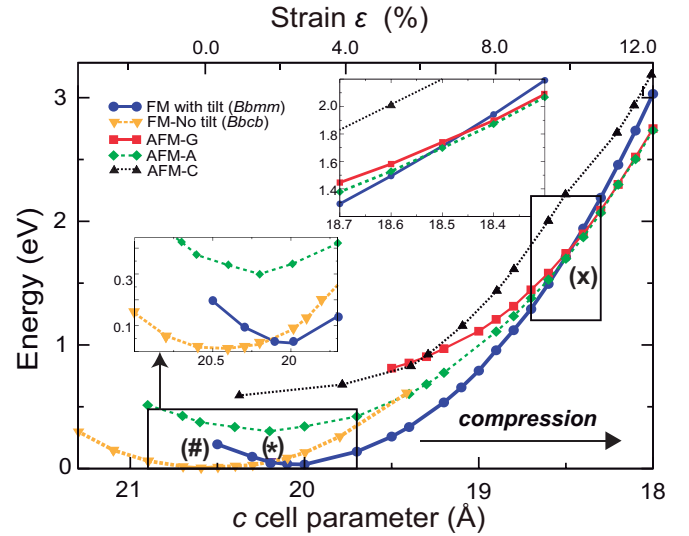
FIG. 2. Energy of FM (with and without tilt), AFM-A, AFM-C, and AFM-G magnetic orderings relative to the FM ground-state energy as a function of decreasing the c lattice parameter. The symbols: (#), (*), and (x) indicate the ground state, first transition (structural), and second transition (electronic and magnetic), respectively.

state, and it does not show much variation in total energy as a function of decreasing the c lattice parameter. This phase is not included in Fig. 2 due to the small energy difference from the FM phase (ΔEI ranges between 0 and 10 meV over the entire range of compressive strains before the transition), which is a consequence of the fact that Ru atoms in different bilayers do not interact significantly. This narrow range of energy differences could indicate the possibility of having a mixed state where bilayers are coupled either ferromagnetically or antiferromagnetically but with all Ru atoms in each bilayer coupled ferromagnetically.

We observe a structural transition from $Bbcb$ to $Bbmm$ that occurs at $c = 20.2$ Å [marked by the symbol (*) in Fig. 2] with the emergence of octahedra tilts and a considerable reduction of rotations (Sec. III B). Further uniaxial compressive strain along the c axis significantly reduces the total energy difference between AFM-A and AFM-G states and the FM phase. At a critical value of $c = 18.5$ Å, a transition from metallic FM to an insulating AFM-A state occurs, corresponding to a compressive strain of approximately 10% [marked by the symbol (x) in Fig. 2]. Further application of compressive strain increases the stability of the AFM-A phase without significant changes in the band gap (Sec. III C).

The FM–AFM-A phase transition has been observed in other systems such as RBaMn$_2$O$_6$ (R = Pr, Nd) [29] or LaMnO$_3$ [30] when temperature goes below the Néel temperature. In those cases the phase transition is associated with the $d_{x^2-y^2}$ orbital order and is consistent with the change in lattice parameters where in-plane parameters are expanded while the out-of-plane parameter is contracted. This result indicates that the FM to AFM-A phase transition could also be generated by applying in-plane tensile strain. In order to gain additional understanding of this phase transition, we analyze in the next section the structural changes induced by the application of
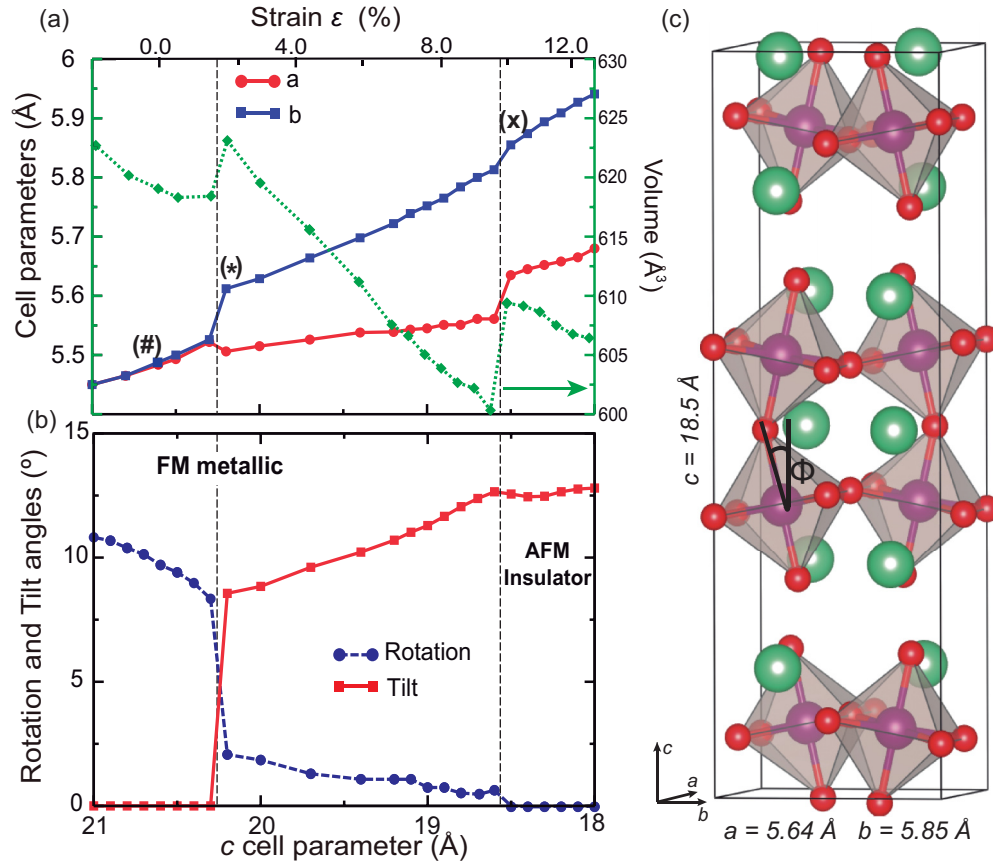
FIG. 3. (a) Evolution of the volume and a and b cell parameters and (b) RuO_6 octahedra rotation and tilts (adapted from Ref. [2]) as a function of reducing the c cell parameter. (c) $Sr_3Ru_2O_7$ structure under 21 GPa of uniaxial pressure where the system is characterized by an insulating AFM state.

compressive strain and their connections with the magnetic phase transition.

B. Structural properties under uniaxial compressive strain

As we apply uniaxial compressive strain along the c axis (making the c parameter shorter), the structural properties of $Sr_3Ru_2O_7$ change. In Fig. 3(a) we show the evolution of the a and b lattice parameters and volume as a function of reducing the c parameter. For small compressive strains ($\epsilon < 2\%$), a and b show the same linear increase with the reduction of c. At a critical compressive strain of $\simeq 2\%$ (where $c = 20.2$ Å and uniaxial pressure is $\simeq 1.5$ GPa) b experiences a sharp elongation of about 0.1 Å, giving rise to uneven in-plane lattice parameters and an increase in volume that yields a larger volume structure than in the ground state. This result is a consequence of the emergence of tilts in the system [Fig. 3(b)]. RuO_6 octahedra become tilted by 8.6°, and the rotations are highly reduced due to the expansion of the in-plane lattice parameters. Further increases in uniaxial compressive strain cause a and b to increase, but with b increasing slightly more than a, indicating a slight anisotropic effect on the structure while octahedra tilts continue increasing and rotations progressively disappear.

Applying uniaxial compressive strain makes the nontilted octahedra in the ground-state structure become tilted by the same amount in all bilayers of the system. This is in contrast to the case when a [001] surface is created in the

system and octahedra tilts emerge only within the first surface bilayer [2].

At $c = 18.5$ Å (10% compressive strain, corresponding to $\simeq 21$ GPa of uniaxial pressure) a second phase transition occurs where the system simultaneously undergoes a FM metallic to an AFM-A insulator transition where tilting of the octahedra increases up to 12.6° and rotations disappear completely. Figure 3(c) shows the top and side views of the resulting structure. During this process, RuO_6 octahedra are transitioning from elongated to compressed, which in combination with the octahedra tilts, is responsible for the electronic and magnetic changes.

From these results we formulate a hypothesis: could expansion of the a and b cell parameters be achieved via in-plane strain producing the same or even new hidden phases? In fact, we have shown that the b lattice parameter increases more than the a lattice parameter, suggesting that tensile strain could efficiently be applied to a particular direction to produce hidden phases with less stress. Before we answer these questions we continue our study on applying compressive strain to analyze the electronic and magnetic properties and how they are connected to the structural changes.

C. Electronic and magnetic properties under uniaxial compressive strain

In Fig. 4(a) we display the evolution of the total energy difference relative to the FM state ($\Delta E = E_{AFM-A} - E_{FM}$)
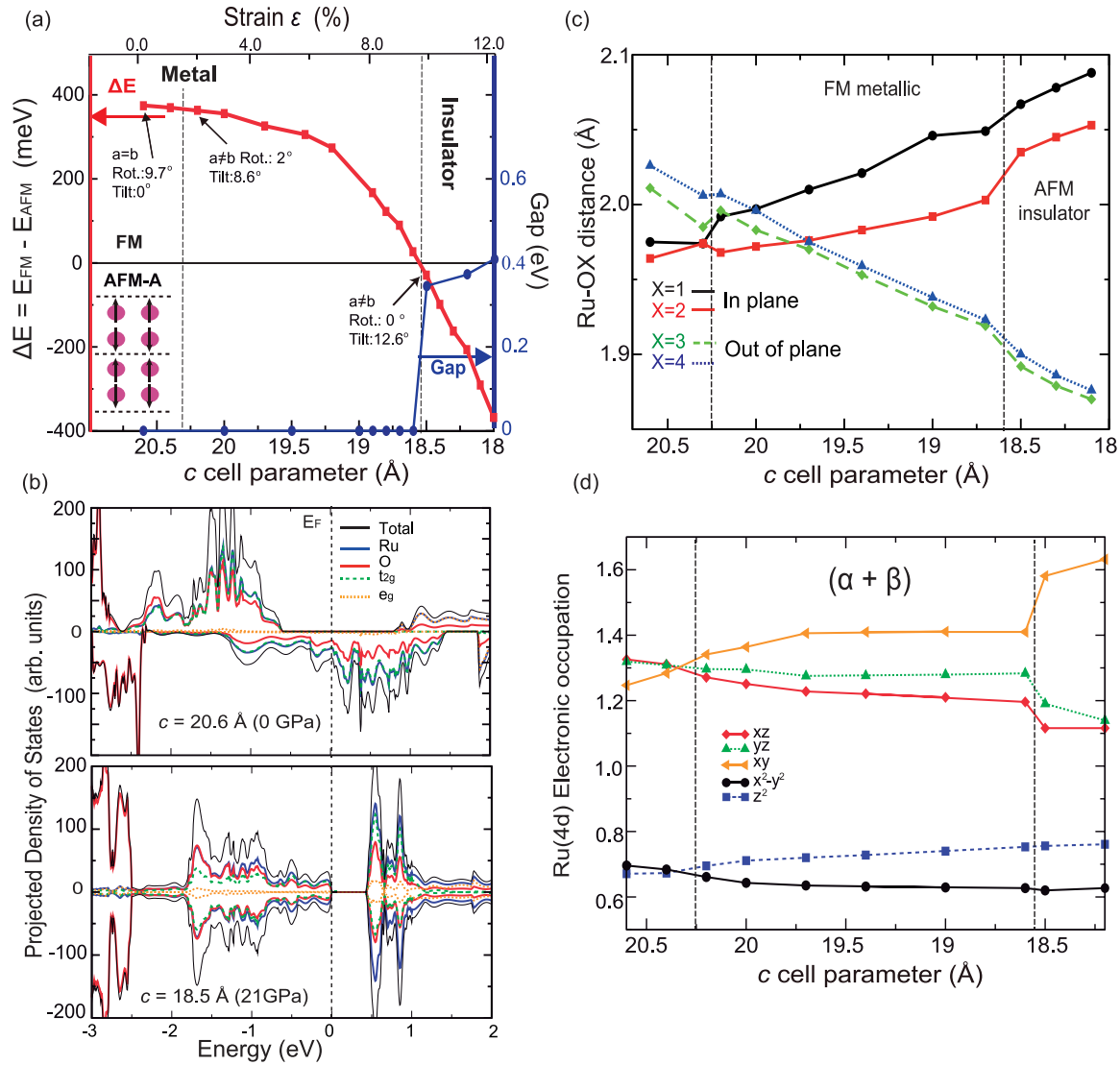
FIG. 4. (a) Phase diagram of $Sr_3Ru_2O_7$ showing the evolution of ΔE and band gap as a function of the c cell parameter and strain (adapted from Ref. [2]). (b) Projected density of states for the FM metallic ground state and AFM-A insulator structures. (c) Evolution of $Ru - OX$ bond distances in the octahedra and (d) evolution of the $Ru(4d)$ electronic occupations ($\alpha + \beta$) as a function of the c lattice parameter (adapted from the Supplemental Material in Ref. [2]).

and band gap as a function of a decreasing c lattice parameter. As can be seen, ΔE decreases from almost 400 to 0 meV as we reduce c from 20.6 to 18.5 Å. At a critical strain of $\epsilon \simeq 10\%$ the FM metallic character of $Sr_3Ru_2O_7$ becomes an insulator with a band gap of $\simeq 0.4$ eV and an A-type AFM configuration. Additional increases in uniaxial compressive strain further stabilize the AFM-A insulating state without significant changes in the band gap. The projected density of states for the FM metallic ground-state structure and the AFM-A insulator state are shown in Fig. 4(b). The ground-state structure features a half-metallic character where t_{2g} electrons participate in the conduction while e_g levels are empty [3].

Figure 4(c) displays the evolution of Ru-O bond distances as a function of a decreasing c parameter through the insulating AFM-A state ($c = 18.5$ Å). We found that RuO_6 octahedra, which were elongated along the c axis in the ground-state, become almost regular (that is, all Ru-O bond distances become

identical) under a uniaxial compressive strain of $\simeq 2\%$ and then compressed under additional strain (Ru-O1 and Ru-O2 bond distances become longer than Ru-O3 and Ru-O4). The compression of the octahedra along with the emergence of and increase in tilts in the system as we apply uniaxial compressive strain has important consequences in the orbital ordering and filling of $Ru(4d)$ and, consequently, affects the electronic and magnetic properties of the compound.

We display in Fig. 4(d) how $Ru(4d)$ electron occupancy ($\alpha + \beta$) evolves as a function of the c lattice parameter. At $c = 20.6$ Å (0 GPa), xz and yz orbitals are doubly degenerate, while xy forms a singlet at higher energy (relative to the doublet), and thus, it is less occupied. This t_{2g} symmetry breaking into a doublet and a singlet is a consequence of the elongated octahedra. The first transition (structural) occurs at $c = 20.2$ Å and leads to a symmetry breaking of the xz and yz orbitals. This occurs along with a crossover where the xy
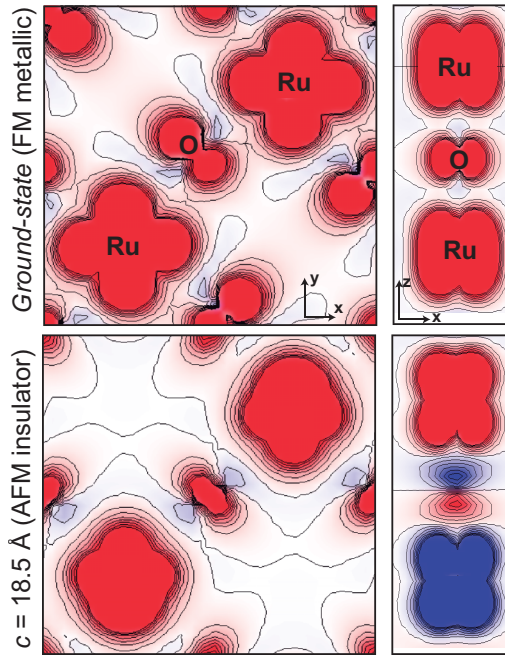
FIG. 5. Charge density of the FM metallic ground-state structure and the AFM insulator state observed under pressure. Different colors indicate different spin orientations.

orbitals are now at a lower energy and more occupied than the xz and yz orbitals. This is a consequence of the emergence of tilts in the system, which changes the polarization between orbitals and therefore the Ru(4d) electron occupancies. This effect can also be seen in the z^2 and x^2-y^2 orbitals (although these orbitals are less populated than t_{2g}). A low-spin state is observed for the entire range of uniaxial strains.

As the uniaxial pressure increases (reduction of the c lattice parameter), the orbital fillings do not show appreciable changes until the metal-to-insulator and magnetic phase transitions occur at $c = 18.5$ Å ($\simeq$21 GPa). At this point, the energy splitting between xy and the xz and yz orbitals increases, leading to a significant change in filling in favor of the xy orbitals. The compressed and tilted RuO$_6$ octahedra under this pressure make the superexchange dominate the Ru-O-Ru out-of-plane interaction, and the system stabilizes in the AFM-A insulating state.

To gain additional insight into this transition we plot in Fig. 5 the charge densities of the FM metallic (ground state) and AFM-A insulating (at $c = 18.5$ Å) structures. Examining these densities allows us to understand how the electrons are arranged in these systems and what orbitals look like. The system under pressure, unlike the ground state, features antiferro-orbital correlations between Ru atoms in plane and out of plane due to the different Ru(d) fillings between xz and yz orbitals. However, the most remarkable feature is in the O atoms connecting octahedra layers along the c axis. Contrary to the ground-state structure, in the system under 21 GPa the O pz orbitals overlap the Ru xz and Ru yz orbitals, leading to an out-of-plane AFM coupling by a superexchange interaction.

We also determined the coupling strength between different neighboring Ru atoms as we applied uniaxial compressive

TABLE II. Magnetic coupling parameters (meV) for different c-axis parameters (Å).

c	J_1	J_2	J_3
20.6[a]	30	51	0.2
19.5	18	31	0.1
18.5	15	−0.7	−0.3
18.1	10	−46	−0.5

[a]Calculated ground-state structure.

strain and compared the results with the ground-state structure. This allowed us to understand the effect of uniaxial pressure on the magnetic property. The magnetic couplings considered here are coupling between Ru nearest neighbors J_1, the coupling between next-nearest neighbors localized out of plane in the bilayer J_2, and the coupling corresponding to the nearest Ru atoms localized in different bilayers J_3 [see Fig. 1(a)]. We calculated these parameters by mapping the energy differences of different spin arrangements to the Ising Hamiltonian [31] as we did in a previous work [3].

The results obtained after solving the equations reported in Ref. [3] can be seen in Table II for the system under different c parameters (different compressive strains). The ground-state structure has an in-plane FM coupling $J_1 > 0$ and an out-of-plane FM coupling $J_2 > 0$. The latter is the strongest coupling in the system (51 meV in comparison to 30 meV for J_1). This can be understood as a consequence of the stronger polarization between Ru and O through the 180° Ru-O-Ru angle in comparison to the 160° Ru-O-Ru angle in plane. As we apply uniaxial compressive strain along the c axis, the system evolves from elongated, nontilted octahedra to tilted, compressed octahedra. This corresponds to breaking the 180° angle between Ru-O-Ru atoms out of plane, making the out-of-plane Ru-O bonds shorter and the in-plane Ru-O bonds longer, ultimately leading to the FM-AFM phase transition.

J_2 is the most sensitive magnetic coupling parameter when uniaxial pressure along the c axis is applied to the structure. This parameter evolves from 51 meV (ground state) to −0.7 meV at the transition (18.5 Å) and down to −46 meV when further compressive strain is applied to the structure. We note that J_3 also changes from FM to AFM character, indicating that AFM-I becomes lower in energy than FM at $c = 18.5$ Å. However, AFM-A is the lowest energetic state when the transition is triggered.

The mechanism associated with the AFM-A insulating phase transition can be understood via the inverse Goodenough-Kanamori interaction [32], in which the Ru-O-Ru intrabilayer angle along the c axis is reduced from 180° to $\simeq$155°, along with a reduction in the corresponding Ru-O bond lengths. This produces a reduction in the magnetic coupling that satisfies the Goodenough-Kanamori rules [33,34], ultimately leading to the FM-AFM phase transition.

We have now tied octahedra distortions to the electronic and magnetic properties of the system. Therefore, we expect that applying in-plane tensile strain will induce similar structural distortions that will eventually trigger phase transitions in the system. One advantage of applying in-plane tensile stress is that one has an extra degree of freedom to use
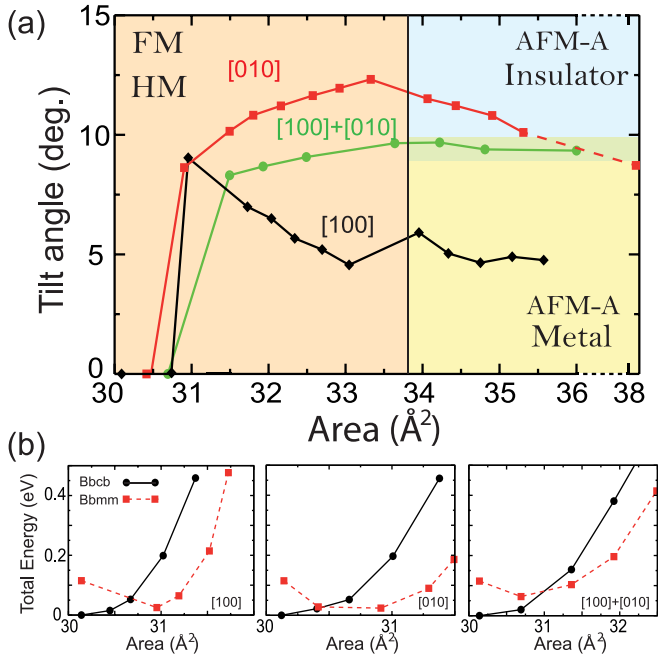
FIG. 6. (a) Evolution of the RuO_6 octahedra tilts as a function of in-plane surface area when tensile strain is applied along [100], [010], and [100]+[010]. The different magnetic and electronic phases highly depend on the tilt of the system. HM stands for half metallic. (b) Total energy difference between the *Bbcb* (nontilted) and *Bbmm* (tilted) symmetries with the ground-state structure as a function of in-plane area in the range of 30 to 32 Å^2.

to manipulate the octahedra in the search for new hidden phases.

D. In-plane tensile stress

The results reported in the previous sections have allowed us to support our hypothesis to apply in-plane tensile strain

to uncover hidden phases in $Sr_3Ru_2O_7$. In this section we analyze the properties of the system when it is under uniaxial and biaxial tensile strain.

In Fig. 6(a) we show the evolution of RuO_6 octahedral tilts as a function of in-plane surface area when tensile strain along [100], [010], and a combination of both (biaxial, [100]+[010]) is applied to the system. The stress produced in all of these cases increases the in-plane area of the system and triggers a structural transition in which octahedra become tilted (as we found by applying compressive strain along the [001] direction). However, the required stress to drive this transition depends on the direction of the application and is lower along [010], reducing the 1.5 GPa obtained with compressive strain to 0.6 GPa. In Fig. 6(b) we display the energetics of the *Bbcb* (nontilted) and *Bbmm* (tilted) symmetry structures as the surface area of the unit cell increases due to the application of tensile strain along different x and y directions. As can be seen, the tilt of the octahedra is a key structural distortion that leads to more stable structures when in-plane tensile strain is applied to the system.

Further application of tensile strain along [010] increases the octahedra tilt up to 12.3°, and the system undergoes a simultaneous electronic and magnetic phase transition similar to the system under uniaxial compressive strain (tilt of 12.6°), but reducing the stress from $\simeq 21$ GPa to 17 GPa. Octahedra find lower energetic structures by tilting along the y axis (rotating about the c axis), and therefore, expanding the system along the [010] direction produces the same effect as compressing along [001], where the b lattice parameter expands more than a (see Sec. III B). The application of tensile stress along [100] or [100]+[010] produces a magnetic phase transition by compressing the octahedra, but the symmetry breaking of the orbitals, induced by tilting, was not large enough to generate the metal-to-insulator phase transition. For these cases we found a nonequilibrium hidden phase characterized by an AFM metallic state. Table III displays the structural parameters and the different predicted phases for each direction where tensile stress is applied.

TABLE III. Structural parameters and magnetic and electronic phases obtained by applying tensile strain along the [100], [010], and biaxial ([100]+[010]) directions. The lattice parameters that were fixed during the calculations are indicated with an asterisk. HM: half metallic, M: metallic, I: insulator.

[100]					[010]					[100]+[010]				
a^* (Å)	b (Å)	c (Å)	Tilt (deg.)	Phase	b^* (Å)	a (Å)	c (Å)	Tilt (deg.)	Phase	a^* (Å)	b^* (Å)	c (Å)	Tilt (deg.)	Phase
5.49	5.49	20.6	0.00	FM/HM	5.49	5.49	20.6	0.00	FM/HM	5.49	5.49	20.6	0.00	FM/HM
5.60	5.57	20.04	0.00	FM/HM	5.55	5.48	20.48	0.00	FM/HM	5.54	5.54	20.37	0.00	FM/HM
5.70	5.53	20.00	0.00	FM/HM	5.60	5.52	20.09	8.60	FM/HM	5.60	5.60	19.99	8.69	FM/HM
5.80	5.47	19.98	6.99	FM/HM	5.70	5.49	20.01	9.53	FM/HM	5.65	5.65	19.91	8.75	FM/HM
5.90	5.43	19.95	6.50	FM/HM	5.80	5.43	19.93	10.15	FM/HM	5.70	5.70	19.78	9.07	FM/HM
6.00	5.39	19.91	5.67	FM/HM	5.90	5.39	19.84	10.82	FM/HM	5.80	5.80	19.58	9.65	AFM/M
6.10	5.36	19.87	5.20	FM/HM	6.00	5.36	19.75	11.21	FM/HM	5.85	5.85	19.25	9.68	AFM/M
6.20	5.33	19.83	4.56	FM/HM	6.10	5.34	19.68	11.64	FM/HM	5.90	5.90	19.14	9.39	AFM/M
6.23	5.45	19.42	5.91	AFM/M	6.20	5.31	19.59	11.95	FM/HM	6.00	6.00	18.98	9.34	AFM/M
6.30	5.45	19.34	5.04	AFM/M	6.30	5.29	19.53	12.32	FM/HM	6.10	6.10	18.82	9.34	AFM/M
6.40	5.43	19.29	4.65	AFM/M	6.32	5.39	19.18	11.51	FM/HM	6.20	6.20	18.68	9.21	AFM/M
6.50	5.41	19.25	4.90	AFM/M	6.40	5.38	19.13	11.22	AFM/I					
6.60	5.39	19.22	4.76	AFM/M	6.50	5.37	19.07	10.81	AFM/I					
					7.20	5.31	18.65	8.35	AFM/I					
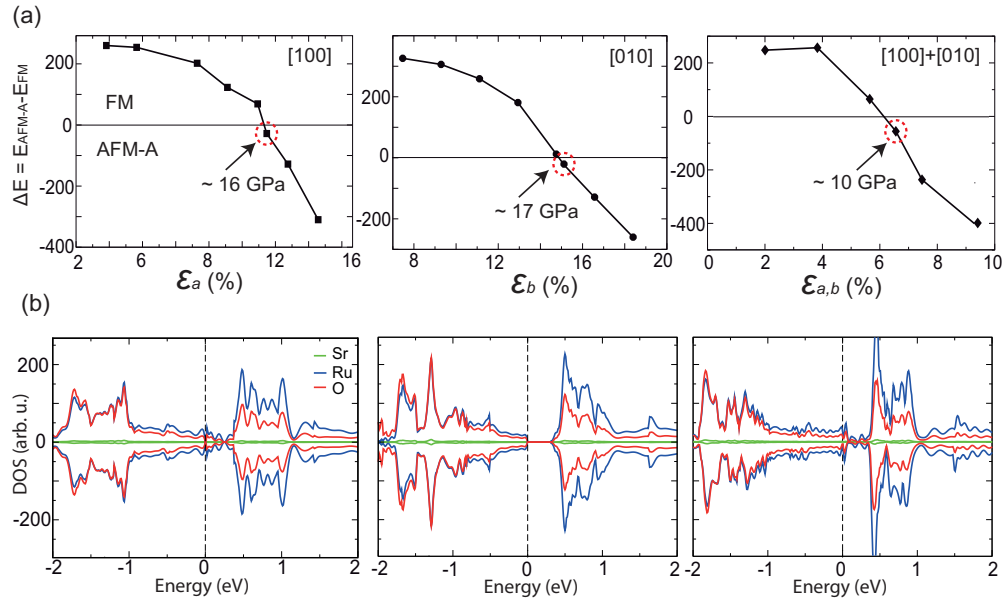
FIG. 7. (a) Evolution of the total energy difference between FM and AFM-A states ($\Delta E = E_{\mathrm{AFM-A}} - E_{\mathrm{FM}}$) as a function of tensile strain along the [100], [010], and [100]+[010] directions. (b) Projected density of states per atom for the AFM-A structures corresponding to the point indicated by a dotted circle in the plot above in (a).

These results suggest that while the evolution of the RuO$_6$ octahedra from elongated to compressed is related to the magnetic phase transition, the octahedral tilts are responsible for the metal-to-insulator transition. To support this idea we applied further tensile strain along the [010] direction to reduce the tilt to 8.35° and thus produce an AFM metallic system (Fig. 6).

In Fig. 7(a) we show the total energy difference between FM and AFM-A states as a function of tensile strain applied along [100], [010], and [100]+[010]. We observe that less strain along [100] ($\simeq$13%) than along the [010] direction ($\simeq$15%) is needed to drive the magnetic phase transition. This indicates

FIG. 8. Magnetic character obtained for structures with different a and b lattice parameters. The size of the circles indicates the absolute value of the ΔE magnitude. The dashed black line corresponds to an in-plane area of 34 Å^2. The larger circle corresponds to $\Delta E = -470$ meV.

the existence of a preferable direction to drive this transition smoothly. The reason for this difference is the different Ru(4d) xz and yz orbital occupations, producing higher resistance to stress along the direction with higher electronic density. The corresponding tensile stress values needed to trigger this transition are 16.1 GPa along the [100] direction and 17.3 GPa along the [010] direction. For the case where we apply biaxial tensile strain, about 6%, corresponding to 9.8 GPa along the [100] direction and 7.4 GPa along the [010] direction, will drive the FM to AFM-A transition in the system. This clearly contrasts with the 21 GPa of compressive stress along the [001] direction needed to drive the magnetic phase transition.

We show in Fig. 7(b) the projected density of states per atom for the AFM phases obtained under minimum strain application along each direction. We observe that only the application of tensile strain along the [010] direction produces a metal-to-insulator transition. In the other two cases the half-metallic character becomes metallic. The reason is the lack of tilt development, as shown in Fig. 6. A detailed analysis of the electronic structure indicates that 4d e_g electronic contributions are responsible for this metallicity, which is related to the filling of electrons at lower energies when tilts are not large enough to break the symmetry of the orbitals that produces the MIT.

Finally, in order to provide a guide for experimentalists to epitaxially grow Sr$_3$Ru$_2$O$_7$ on different-size substrates we provide in Fig. 8 the magnetic state of Sr$_3$Ru$_2$O$_7$ as a function of randomly applying stress along the [100] and [010] directions. The size of the spots represents the total energy differences between FM and AFM states ($\Delta = E_{\mathrm{AFM-A}} - E_{\mathrm{FM}}$). We observe that when the in-plane area, which is associated with a specific combination of compressed and tilted octahedra, becomes larger than 34 Å^2 (represented by the dashed line), the system exhibits an AFM-A phase. Consequently, this shows
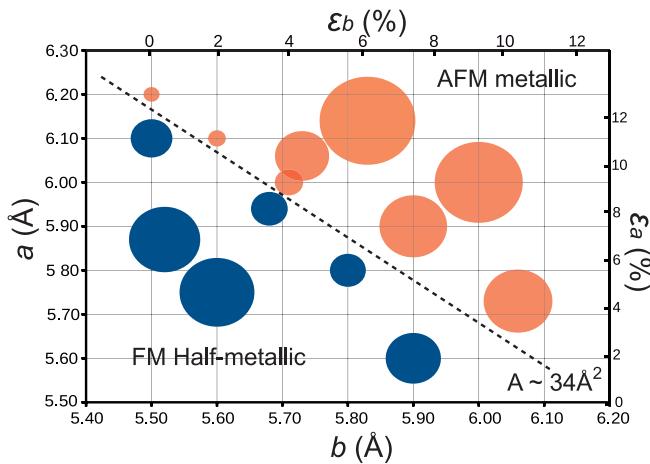
the existence of a clear correlation between in-plane area and magnetic phases.

IV. CONCLUSION

We uncovered an antiferromagnetic metallic hidden phase in $Sr_3Ru_2O_7$ by applying 10 GPa of biaxial tensile strain. The hypothesis that motivated us to apply tensile strain is based on our recently reported results on uniaxial compressive strain along the c axis, where the in-plane lattice parameters increased, yielding two hidden phases. By using hybrid density functional theory we applied uniaxial and biaxial in-plane tensile strains as an alternative procedure. We not only found that these hidden phases were exposed at lower stress but also were able to uncover a hidden phase. Our results indicate that octahedra distortions (tilting, compression, and elongation) can be controlled by applying in-plane tensile strain to expose hidden phases.

[1] C. Chen, J. Kim, V. B. Nascimento, Z. Diao, J. Teng, B. Hu, G. Li, F. Liu, J. Zhang, R. Jin, and E. W. Plummer, Phys. Rev. B **94**, 085420 (2016).

[2] P. Rivero, R. Jin, C. Chen, V. Meunier, E. E. Plummer, and W. Shelton, Sci. Rep. **7**, 10265 (2017).

[3] P. Rivero, V. Meunier, and W. Shelton, Phys. Rev. B **95**, 195106 (2017).

[4] R. S. Perry, L. M. Galvin, S. A. Grigera, L. Capogna, A. J. Schofield, A. P. Mackenzie, M. Chiao, S. R. Julian, S. I. Ikeda, S. Nakatsuji, Y. Maeno, and C. Pfleiderer, Phys. Rev. Lett. **86**, 2661 (2001).

[5] S. A. Grigera, R. S. Perry, A. J. Schofield, M. Chiao, S. R. Julian, G. G. Lonzarich, S. I. Ikeda, Y. Maeno, A. J. Millis, and A. P. Mackenzie, Science **294**, 329 (2001).

[6] P. Steffens, J. Farrell, S. Price, A. P. Mackenzie, Y. Sidis, K. Schmalzl, and M. Braden, Phys. Rev. B **79**, 054422 (2009).

[7] J. Hooper, M. H. Fang, M. Zhou, D. Fobes, N. Dang, Z. Q. Mao, C. M. Feng, Z. A. Xu, M. H. Yu, C. J. O'Connor, G. J. Xu, N. Andersen, and M. Salamon, Phys. Rev. B **75**, 060403 (2007).

[8] G. Li, Q. Li, M. Pan, B. Hu, C. Chen, J. Teng, Z. Diao, J. Zhang, R. Jin, and E. W. Plummer, Sci. Rep. **3**, 2882 (2013).

[9] B. Hu, G. T. McCandless, V. O. Garlea, S. Stadler, Y. Xiong, J. Y. Chan, E. W. Plummer, and R. Jin, Phys. Rev. B **84**, 174411 (2011).

[10] R. Mathieu, A. Asamitsu, Y. Kaneko, J. P. He, X. Z. Yu, R. Kumai, Y. Onose, N. Takeshita, T. Arima, H. Takagi, and Y. Tokura, Phys. Rev. B **72**, 092404 (2005).

[11] J. Peng, Z. Qu, B. Qian, D. Fobes, T. Liu, X. Wu, H. M. Pham, L. Spinu, and Z. Q. Mao, Phys. Rev. B **82**, 024417 (2010).

[12] S.-I. Ikeda, N. Shirakawa, T. Yanagisawa, Y. Yoshida, S. Koikegami, S. Koike, M. Kosaka, and Y. Uwatoko, J. Phys. Soc. Jpn. **73**, 1322 (2004).

[13] W. Wu, A. McCollam, S. A. Grigera, R. S. Perry, A. P. Mackenzie, and S. R. Julian, Phys. Rev. B **83**, 045106 (2011).

[14] M. B. Stone, M. D. Lumsden, R. Jin, B. C. Sales, D. Mandrus, S. E. Nagler, and Y. Qiu, Phys. Rev. B **73**, 174426 (2006).

[15] S. A. Grigera, R. A. Borzi, A. P. Mackenzie, S. R. Julian, R. S. Perry, and Y. Maeno, Phys. Rev. B **67**, 214427 (2003).

[16] H. Shaked, J. Jorgensen, O. Chmaissem, S. Ikeda, and Y. Maeno, J. Solid State Chem. **154**, 361 (2000).

[17] R. Kiyanagi, K. Tsuda, N. Aso, H. Kimura, Y. Noda, Y. Yoshida, S.-I. Ikeda, and Y. Uwatoko, J. Phys. Soc. Jpn. **73**, 639 (2004).

[18] Q. Huang, J. W. Lynn, R. W. Erwin, J. Jarupatrakorn, and R. J. Cava, Phys. Rev. B **58**, 8515 (1998).

[19] R. Dovesi, R. Orlando, A. Erba, C. M. Zicovich-Wilson, B. Civalleri, S. Casassa, L. Maschio, M. Ferrabone, M. D. L. Pierre, P. D'Arco, Y. Noel, M. Causa, M. Rerat, and B. Kirtman, Int. J. Quantum Chem. **114**, 1287 (2014).

[20] R. Dovesi, V. R. Saunders, C. Roetti, R. Orlando, C. M. Zicovich-Wilson, F. Pascale, B. Civalleri, K. Doll, N. M. Harrison, I. J. Bush, P. D'Arco, M. Llunell, M. Caus, and Y. Nol, *CRYSTAL14 User's Manual* (University of Torino, Turin, Italy, 2014).

[21] CRYSTAL basis sets library, http://www.crystal.unito.it/basis-sets.php.

[22] P. J. Hay and W. R. Wadt, J. Chem. Phys. **82**, 299 (1985).

[23] M. Couty and M. B. Hall, J. Comput. Chem. **17**, 1359 (1996).

[24] F. Corà, Mol. Phys. **103**, 2483 (2005).

[25] Z. Wu and R. E. Cohen, Phys. Rev. B **73**, 235116 (2006).

[26] H. J. Monkhorst and J. D. Pack, Phys. Rev. B **13**, 5188 (1976).

[27] R. Ciancio, J. Börjesson, H. Pettersson, R. Fittipaldi, D. Zola, A. Vecchione, M. Polichetti, S. Kittaka, Y. Maeno, S. Pace, and E. Olsson, Phys. Rev. B **80**, 054110 (2009).

[28] K. Jacob, K. T. Lwin, and Y. Waseda, Mater. Sci. Eng. B **103**, 152 (2003).

[29] A. V. Narlikar, *Frontiers in Magnetic Materials* (Springer, Berlin, 2005).

[30] J. B. A. A. Elemans, B. Van Laar, J. R. Van Der Veen, and B. O. Loopstra, J. Solid State Chem. **3**, 238 (1971).

[31] E. Ising, Z. Phys **31**, 253 (1925).

[32] K. Yamaguchi and S. Picozzi, J. Phys.: Condens. Matter **21**, 064203 (2009).

[33] J. B. Goodenough, Phys. Rev. **100**, 564 (1955).

[34] J. Kanamori, J. Phys. Chem. Solids **10**, 87 (1959).